Published in final edited form as:

Inorg Chem. 2020 April 06; 59(7): 5218–5230. doi:10.1021/acs.inorgchem.0c00523.

Inter-Kramers Transitions and Spin–Phonon Couplings in a Lanthanide-Based Single-Molecule Magnet

Duncan H. Moseley,
Department of Chemistry, University of Tennessee, Knoxville, Tennessee 37996, United States

Shelby E. Stavretis,
Department of Chemistry, University of Tennessee, Knoxville, Tennessee 37996, United States

Zhenhua Zhu,
State Key Laboratory of Rare Earth Resource Utilization, Changchun Institute of Applied Chemistry, Chinese Academy of Sciences, Changchun 130022, P. R. China

Mei Guo,
State Key Laboratory of Rare Earth Resource Utilization, Changchun Institute of Applied Chemistry, Chinese Academy of Sciences, Changchun 130022, P. R. China

Craig M. Brown,
Center for Neutron Research, National Institute of Standards and Technology, Gaithersburg, Maryland 20899, United States

Mykhaylo Ozerov,
National High Magnetic Field Laboratory, Tallahassee, Florida 32310, United States

Yongqiang Cheng,
Neutron Scattering Division, Oak Ridge National Laboratory, Oak Ridge, Tennessee 37831, United States

Luke L. Daemen,
Neutron Scattering Division, Oak Ridge National Laboratory, Oak Ridge, Tennessee 37831, United States

Rachael Richardson,

Corresponding Author xue@utk.edu.

Author Contributions

D.H.M., M.O., and D.S. performed the far-IR experiments and interpreted the data. S.E.S., C.M.B., Y.C., L.L.D., and A.J.R.-C. conducted the INS experiments and interpreted the data. S.E.S. and Y.C. performed and analyzed the DFT phonon calculations. D.H.M., K.T., D.S., R.R., G.K., and Z.-L.X. conducted the Raman experiments and interpreted the data. Z.Z., M.G., and J.T. synthesized and characterized compound 1 and grew its crystals for the studies. Z.-L.X. designed and supervised the research and helped with the analyses of the results. D.H.M., S.E.S., and Z.-L.X. wrote the manuscript with input from all authors.

ASSOCIATED CONTENT

Supporting Information

The Supporting Information is available free of charge at https://pubs.acs.org/doi/10.1021/acs.inorgchem.0c00523.

Zeeman splitting of the $M_J = \pm 13/2$ and ±15/2 levels under applied magnetic fields (Figure S1); image of crystals used in far-IR measurements (Figure S2); contour plot of the Spin–Phonon coupling model for ν_3 in far-IR (Figure S6); additional spectra, including far-IR (Figures S3–S7), INS (Figures S8–S9), and Raman (Figure S10); INS spectrum in comparison with calculated phonons (Figure S11); calculated backscattering INS spectrum and peak intensities (Figure S12); Table S2 listing the area and full width at half-maximum of the phonon peak in INS from DCS; and Table S3 listing calculated phonons in $Er[N(SiMe_3)_2]_3$ (1) (PDF)

The authors declare no competing financial interest.

Department of Physics, Florida A&M University, Tallahassee, Florida 32307, United States

Gary Knight,
Department of Physics, Florida A&M University, Tallahassee, Florida 32307, United States

Komalavalli Thirunavukkuarasu,
Department of Physics, Florida A&M University, Tallahassee, Florida 32307, United States

Anibal J. Ramirez-Cuesta,
Neutron Scattering Division, Oak Ridge National Laboratory, Oak Ridge, Tennessee 37831, United States

Jinkui Tang,
State Key Laboratory of Rare Earth Resource Utilization, Changchun Institute of Applied Chemistry, Chinese Academy of Sciences, Changchun 130022, P. R. China

Zi-Ling Xue
Department of Chemistry, University of Tennessee, Knoxville, Tennessee 37996, United States

Abstract

Spin–Phonon coupling plays a critical role in magnetic relaxation in single-molecule magnets (SMMs) and molecular qubits. Yet, few studies of its nature have been conducted. Phonons here refer to both intermolecular and intramolecular vibrations. In the current work, we show Spin–Phonon couplings between IR-active phonons in a lanthanide molecular complex and Kramers doublets (from the crystal field). For the SMM $Er[N(SiMe_3)_2]_3$ (1, Me = methyl), the couplings are observed in the far-IR magnetospectroscopy (FIRMS) of crystals with coupling constants ≈ 2−3 cm^{-1}. In particular, one of the magnetic excitations couples to at least two phonon excitations. The FIRMS reveals at least three magnetic excitations (within the $^4I_{15/2}$ ground state/manifold; hereafter, manifold) at 0 T at 104, ~180, and 245 cm^{-1}, corresponding to transitions from the ground state, $M_J = \pm 15/2$, to the first three excited states, $M_J = \pm 13/2$, ±11/2, and ±9/2, respectively. The transition between the ground and first excited Kramers doublet in 1 is also observed in inelastic neutron scattering (INS) spectroscopy, moving to a higher energy with an increasing magnetic field. INS also gives complete phonon spectra of 1. Periodic DFT computations provide the energies of all phonon excitations, which compare well with the spectra from INS, supporting the assignment of the inter-Kramers doublet (magnetic) transitions in the spectra. The current studies unveil and measure the Spin–Phonon couplings in a typical lanthanide complex and throw light on the origin of the Spin–Phonon entanglement.

Graphical Abstract

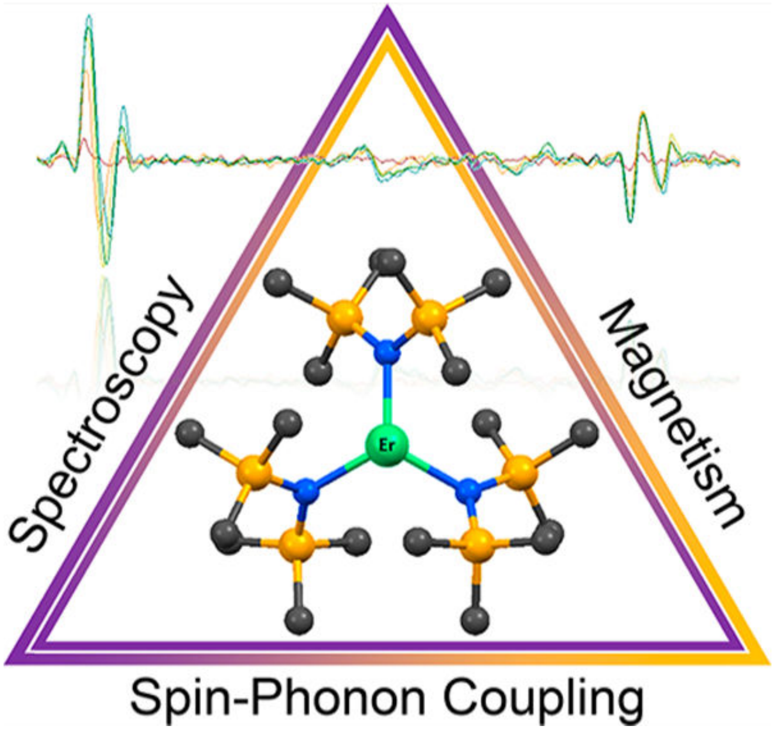

INTRODUCTION

The discovery in the early 1990s that the molecular cluster compound $Mn_{12}O_{12}(OAc)_{16}(H_2O)_4$ ($Mn_{12}Ac$, OAc = acetate) could retain its magnetization for long periods of time in the absence of an external magnetic field[1,2] led to great excitement and intense research in a class of magnetic materials known as single-molecule magnets (SMMs).[3] The strong interest in SMMs stems from their intrinsic properties as molecular analogues of classical bulk ferromagnets and potential applications in, for example, data storage and processing. In 2003, slow magnetic relaxation was reported in mononuclear rare-earth complexes,[4] followed by the observation of similar SMM behaviors in a mononuclear transition metal compound around 2010. These mononuclear compounds of both lanthanides and transition metals form a subclass of SMMs known as single-ion magnets (SIMs).[5–16] Due to their inherent large first-order spin–orbit coupling, lanthanide complexes are described by their total angular momentum (M_J) states as opposed to many transition metal complexes, which are often described by their spin (M_S) states.[7] Interactions between the electron density of the lanthanide ion and the crystal-field environment lead to anisotropies that are required for effective single-ion magnets, as Rinehart and Long had laid out clearly in their study.[5] As a result of the f orbital participation through first-order spin–orbit coupling, the magnetic anisotropy barriers separating the opposite orientations of the spin ground states in lanthanide SIMs tend to be higher than those in the transition metal SIMs which often rely on electronic spin as the only significant source of angular momentum in the compounds. These properties have attracted great interest and extensive work in finding lanthanide SIMs with unique ligands, giving large spin reversal barriers.[4–11,17–26]

There are two requirements for a lanthanide compound to be an effective SIM:[5] (1) The ground state should be doubly degenerate with a high-magnitude quantum number M_J. This is because the bistability ($\pm M_J$) of its ground state is a critical feature of an SIM. In the absence of a magnetic field, breaking the $\pm M_J$ degeneracy is forbidden for a Kramers ion (with an odd electron count). (2) There must be a large separation between the ground and the first excited states. For the f^{11} Er^{3+} ion [$L = 6$, $S = 3/2$, ground-state (or ground-manifold) term symbol $^4I_{15/2}$], Hund's second rule (maximizing orbital angular multiplicity) leads to the ground-state electronic configuration of $4f_{x(x^2-3y^2)}{}^2 4f_{z(x^2-y^2)}{}^2 4f_{xz^2}{}^2 4f_{z^3}{}^2 4f_{yz^2}{}^1 4f_{xyz}{}^1 4f_{y(3x^2-y^2)}{}^1$. With the $4f_{x\left(x^2-3y^2\right)}$ and $4f_{y\left(3x^2-y^2\right)}$ $(m_l = \pm 3)$ orbitals being strongly oblate (equatorially expanded) and the $4f_{z^3}$ orbital ($m_l = 0$) being strongly prolate (axially elongated); the f-electron density of the Er^{3+} ion is thus prolate.[5] An equatorial crystal field is the best to maximize its magnetic anisotropy. Three-coordinated, mononuclear $Er[N(SiMe_3)_2]_3$ (1, Figure 1), initially synthesized by Bradley et al.,[27] has a trigonal pyramidal symmetry, as the single-crystal X-ray diffraction studies by Herrmann et al. showed.[28] The Er^{3+} ion in 1 is slightly above the plane formed by the three amide ligands with C_{3v} symmetry.[28] This complex is the first reported equatorial, Er^{3+}-based SMM.[21,29]

Several Er^{3+} SMMs with equatorial crystal fields have since been studied.[17,18,20,31] The $^4I_{15/2}$ ground manifold in the (ligand-free) Er^{3+} ion (with $2J + 1 = 16$ degenerate states) is split by the crystal field from the three amides into eight doubly degenerate states (known as Kramers doublets) with the ground state of $M_J = \pm 15/2$, as shown in Figure 1. In the C_{3v} crystal field in 1, the x,y directions are equal. The magnetic anisotropy of the compound is from the z direction (known as uniaxial anisotropy). Thus, complex 1 is an especially effective SIM, as the two states in $M_J = \pm 15/2$ are truly degenerate, and the quantum tunneling mechanism (QTM) between them is effectively suppressed.[21]

The separations among the eight Kramers doublets, reflecting the crystal field in 1, are fundamental properties of the compound and important to its ground-state bistability. In particular, the separation between the ground state $M_J = \pm 15/2$ and the first excited state $M_J = \pm 13/2$ is critical to the SIM properties of 1, as indicated earlier. The magnetic relaxation in 1 is believed to be mediated via a higher-energy level by a thermally activated QTM or Orbach process through an excited state.[21] To our knowledge, there have been no *direct* experimental determinations of the separation. Prior to the report of the SIM properties of 1 in 2014, Jank et al. had used a "hot-band" optical absorption technique to determine the energies of inter-Kramers transitions within the $^4I_{15/2}$ manifold, except for the $M_J = \pm 3/2$ and ±1/2 states,[30] by comparing the differences in the *visible* spectra of 1 at 5 and 50 K. For example, the ground state $M_J = \pm 15/2$ is primarily populated at 5 K, giving a peak at 650 nm for the transition from this ground state to a Kramers doublet ($M_J = \pm 7/2$) in the excited state $^4F_{9/2}$ (Figure 1). At 50 K, the first excited state $M_J = \pm 13/2$ becomes populated, i.e., both the $M_J = \pm 15/2$ and $M_J = \pm 13/2$ states are now populated. The transition from the first excited state $M_J = \pm 13/2$ to the Kramers doublet $M_J = \pm 7/2$ in $^4F_{9/2}$, which has a lower energy, is possible. Thus, the visible spectrum shows a new peak (a "hot-band") with a lower energy than the peak at 650 nm. The difference between the new peak and the 650 nm peak, 110 cm^{-1}, was treated as the separation between the ground $M_J = \pm 15/2$ and the first excited $M_J =$

±13/2 states.[30] However, this is an *indirect* method that is not capable of observing the inter-Kramers-doublet transitions directly, and it is thus prone to some degree of error. In the SIM studies for 1, the effective barrier was determined to be 85 cm^{-1} from fitting the ln τ vs T^{-1} data (τ = relaxation time in the AC susceptibility measurement, T = temperature), which is quite a bit lower than the actual excited Kramers doublet; however, it fit well with the computed state.[21] Jank et al. had also calculated the first excited Kramers doublet in 1 to be 82 cm^{-1} by the simulation of the crystal-field splitting pattern.[30] Hallmen et al. have recently conducted *ab initio* calculations of the crystal-field splitting and magnetic properties of 1 by two new approaches: a combination of configuration-averaged Hartree–Fock with the techniques of local-density fitting (LDF-CAHF)[32] and a quasilocal projected internally contracted MRCI (multireference configuration interaction) approach allowing the assessment of the influence of dynamical correlation beyond second-order perturbation theory.[33] Shanmugam et al. have used *ab initio* calculations to give the energies of the low-lying Kramers doublets and to probe the mechanism of magnetic relaxation in 1, showing an unprecedented magnetization blockade up to the third excited state.[34] Results of the calculated levels by different methods (with a range of energies of 82 to ~112 cm^{-1} for the first excited Kramers doublet) have been compared with each other[33] and compared with the experimental results from the "hot-band" method.

Far-IR magnetospectroscopy (FIRMS) has been utilized several times to measure energy levels in lanthanide complexes, and it provides a good measure of the magnetic anisotropy in the system.[35–38] Far-IR is useful for measuring magnetic transitions that are magnetic-and/or electric-dipole allowed. However, this method has rarely been used to study lanthanide-based SMMs, with most of the work performed by van Slageren et al.[39–42] High-field, high-frequency electron paramagnetic resonance (HFEPR) has a typical upper frequency limit of ~33 cm^{-1}, although a few cases exist where HFEPR has been pushed to up to 100 cm^{-1}.[43,44] Thus, HFEPR is often inadequate to study f-element complexes as they typically have energy levels above 100 cm^{-1}. Far-IR spectroscopy allows access to a higher-energy range and is therefore a more suitable method to directly determine the magnetic energy levels in transition metal and lanthanide complexes. For complex 1 in a trigonal crystal field, all of the inter-Kramers transitions within the $^4I_{15/2}$ state in 1 are in theory infrared-active due to the absence of an inversion center.[45]

Another experimental technique is inelastic neutron scattering (INS), which has also occasionally been used to probe magnetic excitations in molecular f-element compounds.[42,46–50] The following methods have been used to distinguish magnetic excitations in INS:[51,52] (1) Unique, different dependences of the magnetic peak and phonon peak intensities on the scattering angles in INS; (2) temperature dependence;[53,54]and (3) diamagnetic controls.[46,47] It should be noted that it may be challenging to find magnetic peaks in samples with large numbers of H atoms by INS spectra from a direct-geometry spectrometer.[51] This is due to the large incoherent scattering cross-section of the H atoms, contributing to strong vibrational intensities that overshadow the magnetic excitation in the INS spectra.[55] Thus, deuterated samples have sometimes been used to help reveal magnetic peaks in the INS spectra,[56,57] as D atoms have a much smaller incoherent scattering cross-section. Typically, a larger amount of sample (e.g., 2.3 g of 1 in the current work and 500 mg in other studies[53,54]) is needed for INS experiments than for far-IR (5–10 mg of 1) or Raman (one single-crystal). Features of the direct-geometry and indirect-geometry INS spectrometers are discussed below. It should also be pointed out that INS is an effective tool to study phonons.[58,59] Unlike with IR and Raman, there are no selection rules for phonons in INS.

Phonons here refer to vibrations of molecular solids, including both external (intermolecular) and internal (intra-molecular) modes. Lattice vibrations are often characterized as external modes, in which the molecules vibrate primarily as a whole with little internal distortion, including translational and librational modes.[60] Significant distortions of atoms that comprise a part of the molecule with a small displacement of the molecular center-of-mass are often called internal modes, commonly known as molecular vibrations.[61] Internal modes typically have much higher frequencies than external modes. From the perspectives of solid-state physics, the internal and external modes originate from the same governing equations and have the same mathematical representations, meaning that both the internal and external modes often couple; thus, all modes are essentially mixed. Therefore, we do not attempt to distinguish the internal and external modes in the current work.

Spin–Phonon coupling, often called spin–lattice relaxation, is the most prevalent mechanism of magnetic relaxation in SMMs.[8,13,14,16,62–67] The coupling of phonons to excited crystal-field states in lanthanide complexes may well lead to additional methods of relaxation. These Spin–Phonon interactions, including their nature and magnitude, are still not clearly understood. Theoretical studies have been recently conducted to understand the relationships between phonons and magnetic relaxations in SMMs.[25,68,69] In addition, a model to calculate optical transitions from a nondegenerated electronic state to a 2-fold degenerated or quasi-degenerated electronic state of molecules with the Jahn–Teller or pseudo-Jahn–Teller effect has been developed by Hizhnyakov and co-workers.[70,71] This method takes into account the vibronic interactions of the metal ion in a complex with two types of vibrations: local vibrations and the vibrations propagating along the crystal (phonons), leading to the symmetry-adapted ligand displacements around the metal ion as a linear superposition of the normal coordinates of the local modes and phonons.[70–73] Rechkemmer et al. have reported Spin–Phonon couplings in a four-coordinate Co^{2+} SIM.[74] We have spectroscopically observed Spin–Phonon couplings as manifested by the avoided crossings in the transition metal SIM $Co(acac)_2(H_2O)_2$ (acac = acetylacetonate) and its isotopologues $Co(acac)_2(D_2O)_2$ and $Co(acac\text{-}d_7)_2(D_2O)_2$ using Raman spectroscopy, where we were able to determine the magnitudes of the couplings among the magnetic excitation and several nearby phonons.[57] Far-IR magnetospectroscopies (FIRMSs) of $Co(acac)_2(H_2O)_2$, $Co(acac)_2(D_2O)_2$, and $Co\text{-}(acac\text{-}d_7)_2(D_2O)_2$ show the magnetic transitions and the magnetic features of Spin–Phonon coupled peaks.[57] The magnetic transitions in the three Co^{2+} SMMs were also probed by INS,[75] and the effect of magnetic fields on the methyl rotation in $Co(acac)_2(D_2O)_2$ was studied.[76] INS and far-IR were also successfully used to investigate the magnetic separation in $[Co(12\text{-crown-}4)_2](I_3)_2(12\text{-crown-}4)$ and its Spin–Phonon coupling.[77]

We report here comprehensive studies of 1 by FIRMS (both crystal and powder samples) and inelastic neutron scattering (INS), showing Spin–Phonon couplings between Kramers doublets in a lanthanide molecular complex and the IR-active phonons that, when fit with a simple model, have coupling constants ≈ 2–3 cm^{-1}. The energies of several Kramers doublets within the $^4I_{15/2}$ ground state in 1 have been directly determined using far-IR and INS spectroscopies. DFT phonon calculations have been performed and are compared with the INS spectra, providing further evidence for magnetic peak determination.

RESULTS AND DISCUSSION

Instrumental properties and sample requirements for the FIRMS and INS experiments in this study are summarized in Table 1.

Far-IR Magnetospectroscopy (FIRMS) Studies.

Magnetic transitions in 1 were studied using far-IR with applied magnetic fields up to 17 T at 5 K using both a crystal mosaic and powder sample. When a magnetic field is applied, each Kramers doublet splits to two energy levels of $+M_J$ and $-M_J$ values (Figure 1 and Figure S1). Depending on the temperature and relative populations, two transitions are possible between the ground and first Kramers doublet: $M_J = -15/2 \rightarrow -13/2$ and $+15/2 \rightarrow +13/2$. Because our far-IR experiments were conducted at 5 K, only the ground state $M_J = -15/2$ is expected to be populated with the applied field. Thus, the $M_J = -15/2 \rightarrow -13/2$ transition is observed. In addition, the separation between the −15/2 and −13/2 states (as well as every other state in the $^4I_{15/2}$ manifold) increases with applied magnetic fields. Thus, the transition shifts to higher energies. When the sample is a crystal, the observed transitions are due to single orientations of the magnetic field with respect to the magnetic anisotropy. In powder samples, the spectra are an average of all of the orientations, and their magnetic transitions thus have a tendency to broaden instead of remaining as clear discrete peaks.

Intramanifold far-IR transitions between the crystal-field split states stemming from a single J-level (Figure 1) have been studied for many systems, although the selection rules for such transitions have yet to be discussed.[80–82] Instead, they are often assumed to be purely magnetic-dipole allowed. Intermanifold transitions have better defined selection rules, and in noncentrosymmetric systems they are allowed by induced electric dipoles due to the mixing of the d and f states.[80]

Upon the application of a field, three far-IR excitations sensitive to magnetic fields appear at 104 and 245 cm^{-1}, referred to henceforth as ν_1 and ν_3, respectively (Figures 3 and 4 for the crystal and powder samples, respectively). A transition between these two is present in the powder spectra at ~180 cm^{-1}, labeled as ν_2 (Figure S5). All three excitations appear to shift to higher energies with an applied magnetic field. In the crystal sample, the magnetic transitions are weak compared to the corresponding excitations in the powder samples. However, all data are consistent. It should be noted that these magnetic peaks exist largely as shoulders or very weak bands in the far-IR spectra. The intense peaks indicated by the dashed red lines in Figure 3 are phonons. The ν_1 transition (assigned to the $M_J = -15/2 \rightarrow -13/2$ transition[30]) is in close agreement with the INS data (*vide infra*). The three peaks agree reasonably well with previously reported data from indirect measurements,[30] with the next two excitations ν_2 and ν_3 assigned as transitions from the ±15/2 ground state to the ±11/2 and ±9/2 excited states, respectively.

Spin–phonon couplings and shift paths are revealed upon close examination of the contour plots of the normalized spectra (Figures 3 and 4), although a visual inspection of the raw transmittance data (Figure 3, top) does not indicate obvious couplings or where peaks are shifting. We speculate that either each of these magnetic excitations or the phonon that they interact with is very weak. A symmetry analysis indicates that a transition from the $M =$ ±15/2 ground state ($\Gamma_{5/6}$ and $E_{3/2}$ in Bethe's and Mulliken's notation, respectively) to any other excited crystal-field state (either $\Gamma_4/E_{1/2}$ or $\Gamma_{5/6}$ in C_{3v}) should be electric-dipole or magnetic-dipole allowed in far-IR spectroscopy in the z ($\Gamma_{5/6}$) and x–y (Γ_4) directions.[30,45,83,84] Both ν_1 and ν_3 experience couplings with at least one observed adjacent phonon (Figure 3).

The ν_1 peak is coupled with a phonon at approximately 112 cm^{-1} (Figure 3, left), causing it to broaden and lose intensity. In other words, both states of the two spin–phonon coupled peaks in Figure 3 (bottom left) contain magnetic and phonon features. Because the phonon here is far-IR-active, the phonon portions of both peaks contribute to the observation of the two peaks. The magnetic transition ν_1 is assigned to be at 104 cm^{-1}, instead of at the 112 cm^{-1} peak, as ν_1 agrees well with the INS results discussed below. In addition, the 104 cm^{-1} peak shifts linearly for the majority of the fields measured but experiences what appears to be an avoided crossing at higher fields. However, the 17 T section of the lower branch in Figure 3 (bottom left), at ~110 cm^{-1}, is not directly on top of the 0 T section of the upper branch at ~112 cm^{-1}. The observation suggests the following: (a) A higher-magnetic field (such as 35 T) may be needed to make the high-field section of the lower branch appear on top of the 0 T section of the upper branch; (b) there is second-order vibronic coupling here, which may shift the first excited-state Kramers doublet $M_J = \pm 13/2$ with the magnetic fields (before the Zeeman effect). The shifts of both the lower and upper branches in Figure 3 (bottom left) may be explained by the second-order vibronic coupling. Alternatively, both the avoided crossing and second-order vibronic coupling perhaps contribute to the observed Spin–Phonon coupling here. Understanding the nature of the Spin–Phonon coupling here is difficult as the Er^{3+} center in the crystal structure is disordered in two positions.[28,30] The disorder prevents the interpretation of the results, including the development of a vibronic coupling model for 1, as was established earlier for $\mathrm{Co(acac)_2(H_2O)_2}$.[57]

If the second-order vibronic coupling is ignored, the coupling in Figure 3 (left) may be modeled by eq 1, consisting of a 2 × 2[57]

$$H = \begin{pmatrix} E_{\mathrm{sp}} & \Lambda \\ \Lambda & E_{\mathrm{ph}} \end{pmatrix} \tag{1}$$

matrix where E_{sp} and E_{ph} are the expected energies of the magnetic and phonon peaks, respectively, prior to coupling; Λ represents the Spin–Phonon coupling constant. Solving the matrix in eq 1 gives two eigenvalues $E_\pm$ (with the avoided-crossing peaks) in the secular eq 2. Since eq 2 involves Λ2, the sign of Λ may not be determined from the far-IR spectra here.

$$\begin{vmatrix} E_{\mathrm{sp}} - E_\pm & \Lambda \\ \Lambda & E_{\mathrm{ph}} - E_\pm \end{vmatrix} = 0 \tag{2}$$

Upon coupling, one state shifts to a higher E_+ while the other shifts to a lower E_-.[85] Fitting the data in Figure 3 (left) by eq 2 yields $|\Lambda| = 3.0(3)$ cm^{-1} with fitting parameters in Table S1.[86]

If the second-order vibronic coupling is included in the consideration, the spin peak position (the lower branch) in Figure 3 (bottom left) may be represented by

$$E_{\mathrm{sp}} = E_0 + CB \tag{3}$$

where E_0 is the peak of the magnetic transition at 0 T (104 cm^{-1}), B is the magnetic field, and C is a constant. Thus, eq 2 becomes

$$\begin{vmatrix} (E_0 + CB) - E_\pm & \Lambda \\ \Lambda & E_{\mathrm{ph}} - E_\pm \end{vmatrix} = 0 \tag{4}$$

Fitting the data in the spectra in Figure 3 (left) by eq 4 yields $|\Lambda| = 2.4(6)$ cm^{-1} and $C = 0.59(5)$ cm^{-1}/T.

The ν_3 peak at 245 cm^{-1} (Figure 3, right) for the $M_J = \pm 15/2 \rightarrow \pm 9/2$ transition at 0 T shows similar features except that it lies between two phonons that it is coupled with *simultaneously*. As ν_3 shifts to higher energies, a lower-energy excitation appears at 242 cm^{-1} at higher fields, originating from ~238 cm^{-1} due to coupling with the magnetic peak. At the higher-magnetic fields of 12–17 T, the intensity of this peak significantly increases due to decreasing Spin–Phonon coupling with the magnetic peak, essentially regaining its original intensity from ν_3. It is likely that the magnetic portion of the excitation is inherently weak in far-IR and is only viewed due to its coupling to phonon transitions, essentially "stealing" their intensity, as observed in the Raman spectra of $Co(acac)_2(H_2O)_2$.[57] Thus, the 253 cm^{-1} excitation becomes too weak to observe after approximately 4 T. If the second-order vibronic coupling is ignored, these three excitations were modeled using a 3 × 3 matrix in eq 5 similar to that in eq 1.

$$H = \begin{pmatrix} E_{\mathrm{sp}} & \Lambda_2 & \Lambda_3 \\ \Lambda_2 & E_{\mathrm{ph2}} & 0 \\ \Lambda_3 & 0 & E_{\mathrm{ph3}} \end{pmatrix} \tag{5}$$

In this equation, E_{sp} is the energy value for an uncoupled ν_3 excitation, E_{ph1} and E_{ph2} are the energies of the two phonons, and Λ_1 and Λ_2 are Spin–Phonon coupling constants with phonons 1 and 2, respectively.

The fitting of the data in Figure 3 (right) yields $\Lambda_2 = 3.0(5)$ cm^{-1} and $\Lambda_3 = 3.0(7)$ cm^{-1} with fitting parameters in Table S1.[86] If the coupled phonons around ν_3 are instead individually modeled using two separate 2 × 2 matrices (Figure S6), the coupling constants are about the same. If the second-order vibronic coupling is included in the fitting here, as in eqs 3 and 4 for the first magnetic transition, the Spin–Phonon coupling constants Λ_2 and Λ_3 are expected to be smaller.

For ν_2 ($M_J = \pm15/2 \rightarrow \pm11/2$ at 0 T, Figure S5) at ~180 cm^{-1}, the changes with the fields are small relative to those of ν_1 and ν_3. The intense phonon at 176 cm^{-1} shifts very slightly to higher energies, likely relaxing back into a pure phonon when ν_2 shifts away. Earlier, the $M_J = \pm15/2 \rightarrow \pm11/2$ transition ν_2 was calculated to be at 145 cm^{-1} and was indirectly observed at 190 cm^{-1} by the "hot-band" technique.[30] Due to the complex structure of the contour plot in Figure S5, it is difficult to say with certainty where the origin of the magnetic peak ν_2 lies. Here, we see a blue region shifting to higher energies, which should correspond to the movement of a valley or a lower-energy excitation. This blue region shifts about 12 cm^{-1}, which is a similar order of magnitude compared to the shifts of ν_1 and ν_3. Thus, it is reasonable to assign the inter-Kramers doublet transition ν as being ~180 cm^{-1} (estimated error: 5 cm^{-1}) at 0 T.

Inelastic Neutron Scattering (INS) Studies.

Two INS studies, one using the Disk Chopper Spectrometer (DCS)[78,87] with variable magnetic fields at the NIST Center for Neutron Research (NCNR) with a 10 T magnet and another using the Vibrational Spectrometer (VISION)[79,88] with variable temperatures at Spallation Neutron Source (SNS), Oak Ridge National Laboratory (ORNL), were conducted for 1 mainly to observe the $M_J = \pm15/2 \rightarrow \pm13/2$ magnetic transition. In addition, VISION spectra give phonons of 1 by INS that are compared with calculated phonons. We have recently reviewed neutron instruments, including DCS and VISION, for research in coordination chemistry.[51]

Each molecule of $Er[N(SiMe_3)_2]_3$ (1) has 54 H atoms. Hydrogen atoms give strong incoherent neutron scattering, leading to background noise in direct-geometry INS spectra.[55] Thus, it is particularly challenging to study the magnetic excitations in 1 in INS by DCS. It should be pointed out that, to our knowledge, neither the perdeuterated ligand $-N(SiMe_3\text{-}d_9)_2$ nor the compound $Er[N(SiMe_3\text{-}d_9)_2]_3$ (**1-*d*$_{54}$**) have been reported.

As a direct-geometry spectrometer,[60,78,87,89] DCS uses multiple choppers to produce a pulsed *monochromatic* neutron beam at the sample. The time-of-flight analyses of scattered neutrons determine energy transfers E between the incident neutron and the sample as well as the scattering vector Q.[51,75,78,87] DCS is limited to energies less than ca. 150 cm^{-1}. One feature relevant to the current research is that a 10 T magnet could be used at DCS, although the magnet itself blocks a number of detectors, leading to the decrease in signal or noise ratios.[75]

At 0 T, we observed the magnetic transition ν_1 in 1 from the ground ($M_J = \pm15/2$) to the first excited state ($M_J = \pm13/2$) at 104 cm^{-1} at 1.7 K. Because the INS experiment was conducted at 1.5 K, only the ground state $M_J = -15/2$ is expected to be populated (Figure 1 and Figure S1). Thus, only the $M_J = -15/2 \rightarrow -13/2$ transition is expected. In addition, the separation between the −15/2 and −13/2 states increases with applied magnetic fields (Figure 5). Thus, the $M_J = -15/2 \rightarrow -13/2$ transition and peak shift to higher energies with applied magnetic fields. This observation is consistent with those from far-IR. At 5 T, the magnetic peak shifted to 105.1 cm^{-1} in the INS (Figure 5). The phonons in the region do not seem to be affected by the application of magnetic fields. At 10 T, the magnetic peak further shifted into the shoulder of a phonon peak, and its energy position could not be accurately determined

(Figure 5). However, both the area and full-width-at-half-maximum (fwhm) of the phonon peak increased at 10 T due to the overlap with the magnetic peak (Table S2).

Unlike DCS, VISION is an inverse-geometry INS spectrometer.[51,60,75,79,88,89] Pulsed, white-beam incident neutrons (with different energies) at high flux are scattered by the sample and then focused onto detectors by crystal analyzer arrays. Such inverse-geometry INS spectrometers typically offer an improved signal-to-noise ratio.[51] For example, the overall inelastic count rate for VISION is more than two orders of magnitude higher than for other similar spectrometers.[79] Currently VISION is *not* equipped with an electromagnet.

The INS spectra of VISION *without* a magnetic field (Figure 6) are similar to the INS spectrum at 0 T of DCS (Figure 5). The magnetic peak at 104 cm^{-1} is visible on the shoulder of a phonon peak at 5 and 25 K. The magnetic peak is expected to disappear with increasing temperatures as Boltzmann statistics predicts. Indeed, the spectra in Figure 6 show that the magnetic peak ν_1 at 104 cm^{-1} disappears by 100 K. Here, Bose correction is used to treat the INS data from VISION. Phonons and electrons are bosons and fermions, respectively, and thus follow Bose–Einstein statistics and Fermi–Dirac statistics, respectively.[75,90] The Bose correction applies a frequency-dependent and temperature-dependent normalization factor such that INS spectra measured at different temperatures are brought to a similar level for comparison. The Bose-corrected spectra at different temperatures are expected to have similar profiles and baseline intensities. The magnetic transition, which does not follow the expected temperature dependence for phonons, will be highlighted for identification. Another feature of VISION is that there are two banks of analyzers with two different scattering angles (represented by |Q| = magnitude of the neutron momentum transfer during the scattering process,[51] |Q| is sometimes represented as Q); one is at 45° (forward scattering, lower |Q|), and another is at 135° (backscattering, higher |Q|), giving two spectra per experimental data acquisition.[51] The magnetic peaks are stronger at small scattering angles (in forward scattering spectra) in INS.[52] Thus, the forward scattering spectra of VISION are shown in Figure 6.

Phonon Calculations and Comparison with Spectra.

The phonons in 1 have been calculated by a periodic DFT method offered by the VASP (Vienna Ab initio Simulation Package).[91] The calculated phonons may be compared with those from the INS experiments. In order to better understand the INS spectra, it is important to be able to assign the peaks to certain vibrational or magnetic excitations. DFT allows for first-principle prediction of interatomic force constants and phonons from electronic structure calculations. The INS spectra, due to vibrational (nonmagnetic) excitations, can then be simulated using the phonon information. Technical details of the calculation can be found in the Experimental Section. The calculated phonons may be compared with those from the INS experiments.

In addition to probing magnetic transitions, INS is an effective tool to probe phonons, including intramolecular vibrations. Unlike optical vibrational spectroscopies such as IR and Raman which are governed by different selection rules, INS does not have selection rules for phonons, as it is based on the kinetic energy transfer between the incident neutrons and the sample.[51,59,89] Using INS to probe phonons has been reviewed by Hudson.[59] By comparing the computed phonon spectra with the experimental INS spectra, magnetic peaks that are *not* in the computed spectra may be revealed.

The reported crystal structure of 1 displays a disorder with the Er^{3+} ion on both sides of the plane formed by the three amide ligands.[28] It is not clear if the disorder is static (C_{3v} symmetry of the complex) or dynamic (D_{3h} symmetry). We have performed DFT calculations to address this issue. Configurations with the Er^{3+} ion on the two different positions were first relaxed to the potential energy minimum. It is found that the separation of the two sites is about 1.5 Å. The potential energy barrier between the two sites was further calculated to be about 250 meV (2016 cm^{-1}) using the nudged elastic band method.[92] These results suggest that the disorder of the Er^{3+} ion is static for the following: (1) Er is a heavy element, and the probability of quantum tunneling over 1.5 Å is essentially zero; (2) the energy barrier is substantially higher than what thermal activation can overcome (with non-negligible probability) at any relevant temperature.

The phonon density-of-states from the INS of 1 seems to match well with those calculated across the entire range, as shown in Figures 7 and 8. A complete list of calculated phonons (for both forwardscattering and backscattering INS) and a list of their symmetries is given in Table S2. The exact positions of the phonons are, however, difficult to calculate, especially at low energies. It should be noted that there are no shoulder peaks representing the magnetic excitation that are calculated, providing further evidence of its nature as a magnetic transition. However, while this supports the assignment of the $M_J = \pm 13/2$ peak, there are little to no indications of any further magnetic peaks in INS. The calculations are expected to help assign the peaks in INS and far-IR spectra.

Comparison of the Far-IR and INS Results.

Results from the far-IR and INS in the current work are compared with the previously reported values by the "hot-band" method in Table 2.[30]

The first inter-Kramers transition peak ν_1 is weak relative to the overlapping phonon, making a direct observation of the peak and its Spin–Phonon couplings in transmittance far-IR spectra (Figure 2 and Figure S3) difficult. However, the far-IR contour plots (Figures 3 and 4, bottom left) clearly reveal the presence of a shifting peak and its Spin–Phonon coupling with an adjacent phonon as an avoided crossing. The third inter-Kramers transition peak ν_3 is much more pronounced at 0 T, residing close to a phonon in transmittance far-IR spectra (Figures 3 and 4, top right), and its Spin–Phonon couplings with adjacent phonons are clear in the far-IR contour plot (Figures 3 and 4, bottom right). The couplings may somewhat alter the positions of ν and ν and alter the neighboring phonons from their ground-state energies. In the magneto-INS of DCS (Figure 5), the magnetic peak is more obvious than in the transmittance far-IR in Figure 2 and Figure S3, and shifting the transition with fields, the peak was identified. In the current studies, DCS probes energy transfers less than 140 cm^{-1}, and thus it was not used to probe ν_2 at ~180 cm^{-1}, ν_3 at 245 cm^{-1}, or any subsequent magnetic excitation. The Spin–Phonon coupling may also not be observable with only a 10 T field (used in INS), as the far-IR contour plot (Figures 3 and 4, bottom left) shows that 10 T is not sufficiently strong to shift the magnetic peak close enough to the phonon to reveal the coupling. It should be pointed out that the far-IR spectrometer used in the current work is coupled to a 17 T magnet.[93] The large magnet in such a sample environment does not block the far-IR detector. In contrast, the sample environment for neutron scattering with the 10 T magnet at DCS requires the placement of the magnet in front of a large number of the detectors,[78] thus blocking the detectors and reducing the signal/noise ratios of the peaks.[75] Therefore, for the magneto-INS studies at DCS, we focused on locating the magnetic/ inter-Kramers transition ν_1. In addition to the direct-geometry DCS with a fixed, selected incident energy E_i and a wide range of **Q** measurement, the indirect-geometry VISION with a "white" incident beam and a much larger flux of the incident neutron beam[51,79] gives a wide energy transfer range with high resolution, albeit limited **Q** information. Although VISION is *not* currently equipped with a magnet, the Bose-corrected VT INS spectra in Figure 6 support the assignment of the magnetic transition ν_1 at 104 cm^{-1}.

Magneto-Raman spectroscopy was used to study 1, but it did not reveal the magnetic peaks, as shown in Figure S10 and discussed in the Supporting Information. It is possible that the air-sensitivity or fluorescence of the sample may have played a role in reducing the effectiveness of the technique. When a vibration (or phonon) leads to a polarizability change in a molecule, the transition is Raman-active. Similarly, if an electronic (or magnetic) transition leads to a polarizability change in a molecule, the transition is also Raman-active.[94] The selection rules for electronic Raman transitions are $\Delta J \leq 2$, $\Delta L \leq 2$, and $\Delta S = 0$.[94–96] However, these rules are likely relaxed under applied magnetic fields due to crystal strain.[96] Intramanifold transitions in lanthanide compounds have been studied by Raman in the past.[94]

CONCLUSION

The current work reports the observation of Spin–Phonon couplings in a lanthanide molecular complex, which are observed as avoided crossings in FIRMS with coupling magnitudes ≈ 2–3 cm^{-1}. In addition, far-IR and INS spectroscopies have been used to quantify the magnetic/Kramers doublet levels in the trigonal pyramidal Er^{3+} compound. They help piece together a picture of these magnetic energy levels and the couplings they experience with neighboring phonons. The studies here are expected to help us understand the magnetic properties of the SIM, including its magnetic relaxations. We believe that the current approach with various complementary spectroscopies could be utilized in the studies of similar f complexes with first-order spin–orbit couplings, assigning inter-Kramers transitions and revealing previously unknown Spin–Phonon couplings. While transitions such as these are not normally expected in corresponding transition metal SIMs without M_J states due to their quenched first-order angular momentum, we believe that any complex with significant spin–orbit couplings should display these transitions in optical spectroscopies.

EXPERIMENTAL SECTION

Complex 1 was synthesized according to a previously reported method.[21,27–29] Instrumental properties and sample requirements for the experiments in this study are summarized in Table 1.

Far-IR Magnetospectroscopy (FIRMS).

Far-IR spectroscopic studies were conducted at the National High Magnetic Field Laboratory (NHMFL) at Florida State University. For far-IR spectra, the powdered samples were dispersed in eicosane in an argon glovebox. Crystal samples were mounted as a mosaic of several needlelike crystals and coated with eicosane in the glovebox to minimize the reaction with air when the samples were later loaded into the 17 T magnet. The spectra were collected at ~4.6 K using a Bruker Vertex 80v FT-IR spectrometer coupled with a 17 T superconducting magnet.

Unlike Raman crystal samples, far-IR samples could be easily mounted in the glovebox and coated with eicosane, as far-IR measures the bulk of the crystal. On the basis of Raman being a surface scattering technique, mounting air-sensitive samples is currently very difficult, because the crystals cannot be coated with eicosane without reducing the effectiveness of the technique.

INS with Variable Fields and Temperatures.

There were two INS studies that were conducted by using different instruments: (a) Variable-magnetic-field (0 to 10 T) INS spectra of 1 at 1.7 K at the time-of-flight DCS were conducted at the NIST Center for Neutron Research (NCNR). This study leads to the identification of the first excited magnetic level with magnetic fields. (b) The variable-temperature INS spectra of 1 were conducted, without a magnet, at VISION at Oak Ridge National Laboratory (ORNL). Both studies used the same powder sample.

At DCS,[87] a 10 T vertical magnet with a dilution refrigerator was used as the sample environment. Inside a helium glovebox, the polycrystalline solid of 1 (2.3 g) was put on a piece of aluminum foil, rolled into a cigar shape, and then wedged and sealed inside an aluminum sample holder so the sample would not move with an applied field. Data were collected at 1.7 K with an incident energy of E_i = 201.6 cm^{-1} (wavelength of 1.81 Å) at 0, 5, and 10 T. In addition, data at 20 K at 0 T were collected, but no significant difference between the spectra at 1.5 and 20 K (0 T) was observed. For DCS, data were collected up to ca. 150 cm^{-1}. All data processing was completed with the Data Analysis and Visualization Environment (DAVE).[97] These INS experiments are particularly challenging, as the distance between the split magnet coils necessitates a smaller neutron beam, leading to the reduction of the incident beam size by a factor of 2.5 and a concomitant shadowing of detectors. This gives ~33% of detector efficiency compared to operations with sample environments such as a cryostat.

After the DCS experiment, the aluminum sample holder was shipped from NCNR to ORNL for variable-temperature INS at VISION. The INS spectra of 1 were measured at 5, 25, 50, 75, and 100 K for 1 h at each temperature without a magnetic field. The VISION,[88] an indirect-geometry instrument,[51] provides data up to 4000 cm^{-1}. The indirect-geometry design for VISION offers two banks of detectors for both the forward (low |Q|) and back (high |Q|) scattering of neutrons.[88] The phonon population effect was corrected by normalizing the INS intensity at the energy transfer ω with coth ($\hbar\omega/2kT$) ($\hbar$ = reduced Planck's constant, k = Boltzmann constant).[58]

VASP Calculation.

Complex 1 crystallizes in space group $P\overline{3}1c$ (No. 163) and has trigonal D_{3d} symmetry.[98] The VASP[91] calculations on 1 were conducted. Geometry optimizations were performed based upon the single-crystal X-ray structure of 1 determined at 293 K. The optimized structure was used for the phonon calculations. Spin-polarized, periodic DFT calculations were performed using the VASP with the projector augmented wave (PAW)[99,100] method and the generalized gradient approximation (GGA)[101] exchange correlation functional with a Hubbard U parameter of 6.5 eV.[102,103] The energy cutoff was 800 eV for the plane–wave basis of the valence electrons. The total energy tolerance for electronic structure minimization was 10^{-8} eV. The optB86b-vdW nonlocal correlation functional that approximately accounts for dispersion interactions was applied.[104] For the structure relaxation, a 2 × 2 × 4 Monkhorst–Pack mesh was applied. Phonopy,[105,106] an open source phonon analyzer, was used to create the 1 × 1 × 2 supercell structure and extract symmetries. The VASP was then employed to calculate the force constants on the supercell in real space using the DFT. Phonopy was not able to assign the doubly degenerated E vibrations for 1. Thus, the calculated E phonons are labeled as both g and u in Table S2.

Supplementary Material

Refer to Web version on PubMed Central for supplementary material.

ACKNOWLEDGMENTS

The authors acknowledge the financial support by the US National Science Foundation (CHE-1633870 and CHE-1900296 to Z.-L.X.), the U.S. Department of Navy HBCU/MI program (K.T.), and a Shull Wollan Center Graduate Research Fellowship (S.E.S). Acknowledgment is also made to the Donors of the American Chemical Society Petroleum Research Fund for partial support of this work. A portion of this work was performed at the National High Magnetic Field Laboratory which is supported by National Science Foundation Cooperative Agreement No. DMR-1644779 and the State of Florida. Neutron scattering experiments were conducted at the VISION beamline at ORNL’s Spallation Neutron Source, which is supported by the Scientific User Facilities Division, Office of Basic Energy Sciences (BES), U.S. Department of Energy (DOE), under Contract No. DE-AC0500OR22725 with UT Battelle, LLC. The computing resources were made available through the VirtuES and the ICEMAN projects, funded by Laboratory Directed Research and Development program and Compute and Data Environment for Science (CADES) at ORNL. The authors thank Dr. Dmitry Smirnov and Zhengguang Lu for assistance.

REFERENCES

(1). Sessoli R; Tsai HL; Schake AR; Wang S; Vincent JB; Folting K; Gatteschi D; Christou G; Hendrickson DN High-spin molecules: [Mn12O12(O2CR)16(H2O)4]. J. Am. Chem. Soc 1993, 115, 1804–1816.

(2). Sessoli R; Gatteschi D; Caneschi A; Novak MA Magnetic bistability in a metal-ion cluster. Nature 1993, 365, 141–143.

(3). Gatteschi D; Sessoli R Quantum Tunneling of Magnetization and Related Phenomena in Molecular Materials. Angew. Chem., Int. Ed 2003, 42, 268–297.

(4). Ishikawa N; Sugita M; Ishikawa T; Koshihara S.-y.; Kaizu Y Lanthanide Double-Decker Complexes Functioning as Magnets at the Single-Molecular Level. J. Am. Chem. Soc 2003, 125, 8694–8695. [PubMed: 12862442]

(5). Rinehart JD; Long JR Exploiting Single-Ion Anisotropy in the Design of f-Element Single-Molecule Magnets. Chem. Sci 2011, 2, 2078–2085.

(6). Woodruff DN; Winpenny REP; Layfield RA Lanthanide Single-Molecule Magnets. Chem. Rev 2013, 113, 5110–5148. [PubMed: 23550940]

(7). Liddle ST; van Slageren J Improving f-Element Single Molecule Magnets. Chem. Soc. Rev 2015, 44, 6655–6669. [PubMed: 26158197]

(8). Zhang P; Zhang L; Tang J Lanthanide single molecule magnets: Progress and perspective. Dalton Trans 2015, 44, 3923–3929. [PubMed: 25641200]

(9). Lu J; Guo M; Tang J Recent Developments in Lanthanide Single-Molecule Magnets. Chem. - Asian J 2017, 12, 2772–2779. [PubMed: 28862379]

(10). Liu J-L; Chen Y-C; Tong M-L Symmetry Strategies for High Performance Lanthanide-Based Single-Molecule Magnets. Chem. Soc. Rev 2018, 47, 2431–2453. [PubMed: 29492482]

(11). Feng M; Tong M-L Single Ion Magnets from 3d to 5f: Developments and Strategies. Chem. - Eur. J 2018, 24, 7574–7594. [PubMed: 29385282]

(12). Craig GA; Murrie M 3d single-ion magnets. Chem. Soc. Rev 2015, 44, 2135–2147. [PubMed: 25716220]

(13). Frost JM; Harriman KLM; Murugesu M The rise of 3-d single-ion magnets in molecular magnetism: towards materials from molecules? Chem. Sci 2016, 7, 2470–2491. [PubMed: 28660017]

(14). Molecular Nanomagnets and Related Phenomena; Gao S, Ed.; Springer, 2015.

(15). Feltham HLC; Brooker S Review of Purely 4f and Mixed-Metal nd-4f Single-Molecule Magnets Containing only One Lanthanide Ion. Coord. Chem. Rev 2014, 276, 1–33.

(16). Layfield RA Organometallic Single-Molecule Magnets. Organometallics 2014, 33, 1084–1099.

(17). Jiang S-D; Wang B-W; Sun H-L; Wang Z-M; Gao S An Organometallic Single-Ion Magnet. J. Am. Chem. Soc 2011, 133, 4730–4733. [PubMed: 21401130]

(18). Meihaus KR; Long JR Magnetic Blocking at 10 K and a Dipolar-Mediated Avalanche in Salts of the Bis(η8-cyclooctatetraenide) Complex [Er(COT)2]−. J. Am. Chem. Soc 2013, 135, 17952–17957. [PubMed: 24188004]

(19). Le Roy JJ; Korobkov I; Murugesu M A Sandwich Complex with Axial Symmetry for Harnessing the Anisotropy in a Prolate Erbium(III) Ion. Chem. Commun 2014, 50, 1602–1604.

(20). Palacios MA; Titos-Padilla S; Ruiz J; Herrera JM; Pope SJA; Brechin EK; Colacio E Bifunctional $Zn^{II}Ln^{III}$ Dinuclear Complexes Combining Field Induced SMM Behavior and Luminescence: Enhanced NIR Lanthanide Emission by 9-Anthracene Carboxylate Bridging Ligands. Inorg. Chem 2014, 53, 1465–1474. [PubMed: 24341473]

(21). Zhang P; Zhang L; Wang C; Xue S; Lin S-Y; Tang J Equatorially Coordinated Lanthanide Single Ion Magnets. J. Am. Chem. Soc 2014, 136, 4484–4487. [PubMed: 24625001]

(22). Chen Y-C; Liu J-L; Ungur L; Liu J; Li Q-W; Wang L-F; Ni Z-P; Chibotaru LF; Chen X-M; Tong M-L Symmetry-Supported Magnetic Blocking at 20 K in Pentagonal Bipyramidal Dy(III) Single-Ion Magnets. J. Am. Chem. Soc 2016, 138, 2829–2837. [PubMed: 26883386]

(23). Liu J; Chen Y-C; Liu J-L; Vieru V; Ungur L; Jia J-H; Chibotaru LF; Lan Y; Wernsdorfer W; Gao S; Chen X-M; Tong M-L A Stable Pentagonal Bipyramidal Dy(III) Single-Ion Magnet with a Record Magnetization Reversal Barrier over 1000 K. J. Am. Chem. Soc 2016, 138, 5441–5450. [PubMed: 27054904]

(24). Chen YC; Liu JL; Wernsdorfer W; Liu D; Chibotaru LF; Chen XM; Tong ML Hyperfine-Interaction-Driven Suppression of Quantum Tunneling at Zero Field in a Holmium(III) Single-Ion Magnet. Angew. Chem., Int. Ed 2017, 56, 4996–5000.

(25). Goodwin CAP; Ortu F; Reta D; Chilton NF; Mills DP Molecular Magnetic Hysteresis at 60 K in Dysprosocenium. Nature 2017, 548, 439. [PubMed: 28836589]

(26). Guo FS; Day BM; Chen YC; Tong ML; Mansikkamäki A; Layfield RA A Dysprosium Metallocene Single-Molecule Magnet Functioning at the Axial Limit. Angew. Chem., Int. Ed 2017, 56, 11445–11449.

(27). Bradley DC; Ghotra JS; Hart FA Three-co-ordination in lanthanide chemistry: tris[bis(trimethylsilyl)amido]lanthanide(III) compounds. J. Chem. Soc., Chem. Commun 1972, 349–350.

(28). Herrmann WA; Anwander R; Munck FC; Scherer W; Dufaud V; Huber NW; Artus GRJ Reaktivitaẗsbestimmender Einfluß der Ligandenkonstitution bei Seltenerdamiden: Herstellung und Struktur sterisch überladener Alkoxid-Komplexe. Z. Naturforsch., B: J. Chem. Sci 1994, 49b, 1789–1797.

(29). Zhang P; Jung J; Zhang L; Tang J; Le Guennic B Elucidating the Magnetic Anisotropy and Relaxation Dynamics of Low-Coordinate Lanthanide Compounds. Inorg. Chem 2016, 55, 1905–1911. [PubMed: 26812039]

(30). Jank S; Amberger HD; Edelstein NM Electronic Structures of Highly-Symmetrical Compounds of f Elements: Part 30. Simulation of the Crystal Field Splitting Pattern of Tris(bis-(trimethylsilyl)amido)erbium (III). Spectrochim. Acta, Part A 1998, 54, 1645–1650.

(31). AlDamen MA; Clemente-Juan JM; Coronado E; Martí-Gastaldo C; Gaita-Ariño, A. Mononuclear Lanthanide Single-Molecule Magnets Based on Polyoxometalates. J. Am. Chem. Soc 2008, 130, 8874–8875. [PubMed: 18558687]

(32). Hallmen PP; Köppl C; Rauhut G; Stoll H; van Slageren J Fast and reliable *ab initio* calculation of crystal field splittings in lanthanide complexes. J. Chem. Phys 2017, 147, 164101. [PubMed: 29096514]

(33). Hallmen PP; Rauhut G; Stoll H; Mitrushchenkov AO; van Slageren J Crystal Field Splittings in Lanthanide Complexes: Inclusion of Correlation Effects beyond Second Order Perturbation Theory. J. Chem. Theory Comput 2018, 14, 3998–4009. [PubMed: 29906105]

(34). Singh SK; Gupta T; Shanmugam M; Rajaraman G Unprecedented Magnetic Relaxation via the Fourth Excited State in Low-Coordinate Lanthanide Single-Ion Magnets: A Theoretical Perspective. Chem. Commun 2014, 50, 15513–15516.

(35). Hill JC; Wheeler RG Far-Infrared Spectra of Erbium, Dysprosium, and Samarium Ethyl Sulphate. Phys. Rev 1966, 152, 482–494.

(36). Bloor D; Copland GM Far Infrared Spectra of Magnetic Ions in Crystals. Rep. Prog. Phys 1972, 35, 1173.

(37). Sievers AJ; Tinkham M Far Infrared Spectra of Rare-Earth Iron Garnets. Phys. Rev 1963, 129, 1995–2004.

(38). Hadni A; Morlot G; Strimer P Far-Infrared Electronic Transitions in Solids. IEEE J. Quantum Electron 1967, 3, 111–116.

(39). Slota M; Jiang S-D; Heintze E; Rechkemmer Y; Dressel M; van Slageren J; Bogani L Accurate and Unequivocal Determination of the Crystal-Field Parameters of Lanthanide Ions via a Multitechnique Approach. Phys. Rev. B: Condens. Matter Mater. Phys 2019, 99, 134410.

(40). Perfetti M; Gysler M; Rechkemmer-Patalen Y; Zhang P; Taştan H; Fischer F; Netz J; Frey W; Zimmermann LW; Schleid T; Hakl M; Orlita M; Ungur L; Chibotaru L; Brock-Nannestad T; Piligkos S; van Slageren J Determination of the Electronic Structure of a Dinuclear Dysprosium Single Molecule Magnet without Symmetry Idealization. Chem. Sci 2019, 10, 2101–2110. [PubMed: 30842867]

(41). Rechkemmer Y; Fischer JE; Marx R; Dörfel M; Neugebauer P; Horvath S; Gysler M; Brock-Nannestad T; Frey W; Reid MF; van Slageren J Comprehensive Spectroscopic Determination of the Crystal Field Splitting in an Erbium Single-Ion Magnet. J. Am. Chem. Soc 2015, 137, 13114–13120. [PubMed: 26394012]

(42). Marx R; Moro F; Dorfel M; Ungur L; Waters M; Jiang SD; Orlita M; Taylor J; Frey W; Chibotaru LF; van Slageren J Spectroscopic Determination of Crystal Field Splittings in Lanthanide Double Deckers. Chem. Sci 2014, 5, 3287–3293.

(43). Zvyagin SA; Ozerov M; Čizmǎŕ E; Kamenskyi D; Zherlitsyn S; Herrmannsdörfer T; Wosnitza J; Wünsch R; Seidel W Terahertz-Range Free-Electron Laser Electron Spin Resonance Spectroscopy: Techniques and Applications in High Magnetic Fields. Rev. Sci. Instrum 2009, 80, 073102. [PubMed: 19655938]

(44). Ozerov M; Bernáh B; Kamenskyi D; Redlich B; van der Meer AFG; Christianen PCM; Engelkamp H; Maan JC A THz Spectrometer Combining the Free Electron Laser FLARE with 33 T Magnetic Fields. Appl. Phys. Lett 2017, 110, 094106.

(45). Cotton FA Chemical Applications of Group Theory, 3rd ed.; Wiley: New York, 1971.

(46). Pedersen KS; Ungur L; Sigrist M; Sundt A; Schau-Magnussen M; Vieru V; Mutka H; Rols S; Weihe H; Waldmann O; Chibotaru LF; Bendix J; Dreiser J Modifying the Properties of 4f Single-Ion Magnets by Peripheral Ligand Functionalisation. Chem. Sci 2014, 5, 1650–1660.

(47). Pedersen KS; Dreiser J; Weihe H; Sibille R; Johannesen HV; Sørensen MA; Nielsen BE; Sigrist M; Mutka H; Rols S; Bendix J; Piligkos S Design of Single-Molecule Magnets: Insufficiency of the Anisotropy Barrier as the Sole Criterion. Inorg. Chem 2015, 54, 7600–7606. [PubMed: 26201004]

(48). Urland W; Kremer R; Furrer A Crystal Field Levels in Tetraphenylarsoniumpentakis(nitrato)ytterbate(III) Determined by Neutron Spectroscopy. Chem. Phys. Lett 1986, 132, 113–115.

(49). Baker ML; Tanaka T; Murakami R; Ohira-Kawamura S; Nakajima K; Ishida T; Nojiri H Relationship between Torsion and Anisotropic Exchange Coupling in a Tb^{III}-Radical-Based Single-Molecule Magnet. Inorg. Chem 2015, 54, 5732–5738. [PubMed: 26010987]

(50). Dunstan MA; Mole RA; Boskovic C Inelastic Neutron Scattering of Lanthanoid Complexes and Single-Molecule Magnets. Eur. J. Inorg. Chem 2019, 2019, 1090–1105.

(51). Xue Z-L; Ramirez-Cuesta AJ; Brown CM; Calder S; Cao H; Chakoumakos BC; Daemen LL; Huq A; Kolesnikov AI; Mamontov E; Podlesnyak AA; Wang X Neutron Instruments for Research in Coordination Chemistry. Eur. J. Inorg. Chem 2019, 2019, 1065–1089.

(52). Bacon GE Neutron Scattering in Chemistry; Butterworth: London, 1977.

(53). Stavretis SE; Atanasov M; Podlesnyak AA; Hunter SC; Neese F; Xue Z-L Magnetic transitions in iron porphyrin halides by inelastic neutron scattering and ab initio studies of zero-field splittings. Inorg. Chem 2015, 54, 9790–9801. [PubMed: 26428688]

(54). Hunter SC; Podlesnyak AA; Xue Z-L Magnetic excitations in metalloporphyrins by Inelastic Neutron Scattering: Determination of zero-field splittings in iron, manganese, and chromium complexes. Inorg. Chem 2014, 53, 1955–1961. [PubMed: 24527685]

(55). Furrer A; Mesot J; Strässle T Neutron Scattering in Condensed Matter Physics; World Scientific, 2009.

(56). Dobe C; Strässle T; Juranyi F; Tregenna-Piggott PLW Pressure-Induced Switch of the Direction of the Unique Jahn-Teller Axis of the Chromium(II) Hexaqua Cation in the Deuterated Ammonium Chromium Tutton Salt. Inorg. Chem 2006, 45, 5066–5072. [PubMed: 16780328]

(57). Moseley DH; Stavretis SE; Thirunavukkuarasu K; Ozerov M; Cheng Y; Daemen LL; Ludwig J; Lu Z; Smirnov D; Brown CM; Pandey A; Ramirez-Cuesta AJ; Lamb AC; Atanasov M; Bill E; Neese F; Xue Z-L; et al. Spin–Phonon Couplings in Transition Metal Complexes with Slow Magnetic Relaxation. Nat. Commun 2018, 9, 2572. [PubMed: 29968702]

(58). Mitchell PCH; Parker SF; Ramirez-Cuesta AJ; Tomkinson J Vibrational Spectroscopy with Neutrons: With Applications in Chemistry, Biology, Materials Science and Catalysis; World Scientific Publishing Company, 2005; Vol. 3.

(59). Hudson BS Vibrational Spectroscopy via Inelastic Neutron Scattering. In Frontiers of Molecular Spectroscopy; Laane J, Ed.; Elsevier: Amsterdam, 2009, pp 597–622.

(60). Mitchell PCH; Parker SF; Ramirez-Cuesta AJ; Tomkinson J Vibrational Spectroscopy with Neutrons: With Applications in Chemistry, Biology, Materials Science and Catalysis; World Scientific Publishing Company, 2005.

(61). Dove MT Introduction to Lattice Dynamics; Cambridge Topics in Mineral Physics and Chemistry; Cambridge University Press, 1993.

(62). Benelli C; Gatteschi D Single Ion Magnet (SIM). In Introduction to Molecular Magnetism; Wiley-VCH, 2015; pp 217–237.

(63). Krzystek J; Telser J Measuring giant anisotropy in paramagnetic transition metal complexes with relevance to single-ion magnetism. Dalton Trans 2016, 45, 16751–16763. [PubMed: 27722619]

(64). McInnes EJL; Winpenny REP Molecular Magnets. In Comprehensive Inorganic Chemistry II; Poeppelmeier K, Ed.; Elsevier: Amsterdam, 2013; pp 371–395.

(65). Neese F; Pantazis DA What is not required to make a single molecule magnet. Faraday Discuss 2011, 148, 229–238. [PubMed: 21322486]

(66). Demir S; Jeon I-R; Long JR; Harris TD Radical ligand-containing single-molecule magnets. Coord. Chem. Rev 2015, 289, 149–176.

(67). Orbach R; Stapleton HJ Electron Spin-Lattice Relaxation. In Electron Paramagnetic Resonance; Geschwind S, Ed.; Plenum Press: New York, 1972; pp 121–216.

(68). Lunghi A; Totti F; Sanvito S; Sessoli R Intra-Molecular Origin of the Spin-Phonon Coupling in Slow-Relaxing Molecular Magnets. Chem. Sci 2017, 8, 6051–6059. [PubMed: 28989635]

(69). Escalera-Moreno L; Suaud N; Gaita-Ariño A; Coronado E Determining Key Local Vibrations in the Relaxation of Molecular Spin Qubits and Single-Molecule Magnets. J. Phys. Chem. Lett 2017, 8, 1695–1700. [PubMed: 28350165]

(70). Hizhnyakov V; Pae K; Vaikjař T Optical Jahn–Teller effect in the case of local modes and phonons. Chem. Phys. Lett 2012, 525–526, 64–68.

(71). Pae K; Hizhnyakov V Nonadiabaticity in a Jahn-Teller system probed by absorption and resonance Raman scattering. J. Chem. Phys 2013, 138, 104103. [PubMed: 23514461]

(72). Palii A; Ostrovsky S; Reu O; Tsukerblat B; Decurtins S; Liu S-X; Klokishner S Microscopic theory of cooperative spin crossover: Interaction of molecular modes with phonons. J. Chem. Phys 2015, 143, 084502. [PubMed: 26328851]

(73). Palii A; Ostrovsky S; Reu O; Tsukerblat B; Decurtins S; Liu S-X; Klokishner S Diversity of Spin Crossover Transitions in Binuclear Compounds: Simulation by Microscopic Vibronic Approach. J. Phys. Chem. C 2016, 120, 14444–14453.

(74). Rechkemmer Y; Breitgoff FD; van der Meer M; Atanasov M; Hakl M; Orlita M; Neugebauer P; Neese F; Sarkar B; van Slageren J; et al. A Four-Coordinate Cobalt(II) Single-Ion Magnet with Coercivity and a Very High Energy Barrier. Nat. Commun 2016, 7, 10467. [PubMed: 26883902]

(75). Stavretis SE; Cheng Y; Daemen LL; Brown CM; Moseley DH; Bill E; Atanasov M; Ramirez-Cuesta AJ; Neese F; Xue Z-L Probing Magnetic Excitations in Co^{II} Single-Molecule Magnets by Inelastic Neutron Scattering. Eur. J. Inorg. Chem 2019, 2019, 1119–1127.

(76). Stavretis SE; Mamontov E; Moseley DH; Cheng Y; Daemen LL; Ramirez-Cuesta AJ; Xue Z-L Effect of magnetic fields on the methyl rotation in a paramagnetic cobalt(II) complex. Quasielastic neutron scattering studies. Phys. Chem. Chem. Phys 2018, 20, 21119–21126. [PubMed: 30079409]

(77). Stavretis SE; Moseley DH; Fei F; Cui H-H; Cheng Y; Podlesnyak AA; Wang X; Daemen LL; Hoffmann CM; Ozerov M; Lu Z; Thirunavukkuarasu K; Smirnov D; Chang T; Chen Y-S; Ramirez-Cuesta AJ; Chen X-T; Xue Z-L Spectroscopic Studies of the Magnetic Excitation and Spin-Phonon Couplings in a Single-Molecule Magnet. Chem. - Eur. J 2019, 25, 15846–15857. [PubMed: 31529652]

(78). DCS website. https://ncnr.nist.gov/instruments/dcs/.

(79). VISION website. https://neutrons.ornl.gov/vision.

(80). Görller-Walrand C; Binnemans K Handbook on the Physics and Chemistry of Rare Earths; Gschneider KA, Eyring L, Eds.; Elsevier: Amsterdam, 1998; Vol. 25, pp 101–264.

(81). Rogers PD; Choi YJ; Standard EC; Kang TD; Ahn KH; Dubroka A; Marsik P; Wang C; Bernhard C; Park S; Cheong SW; Kotelyanskii M; Sirenko AA Adjusted oscillator strength matching for hybrid magnetic and electric excitations in $Dy_3Fe_5O_{12}$ garnet. Phys. Rev. B: Condens. Matter Mater. Phys 2011, 83, 174407.

(82). Sirenko AA; O'Malley SM; Ahn KH; Park S; Carr GL; Cheong SW Infrared-active excitations related to Ho^{3+} ligand-field splitting at the commensurate-incommensurate magnetic phase transition in HoMn2O5. Phys. Rev. B: Condens. Matter Mater. Phys 2008, 78, 174405.

(83). Koster GF; Dimmock JO; Wheeler RG; Statz H Properties of the Thirty-Two Point Groups; MIT Press, 1963; p 51.

(84). Jacobs PWM Group Theory with Applications in Chemical Physics; Cambridge University Press, 2005; p 447.

(85). Cohen-Tannoudji C; Laloë F; Diu B Quantum Mechanics; Wiley: New York, 1977; Vol. 1.

(86). Frank W; von Brentano P Classical Analogy to Quantum Mechanical Level Repulsion. Am. J. Phys 1994, 62, 706–709.

(87). Copley JRD; Cook JC The Disk Chopper Spectrometer at NIST: A New Instrument for Quasielastic Neutron Scattering Studies. Chem. Phys 2003, 292, 477–485.

(88). Seeger PA; Daemen LL; Larese JZ Resolution of VISION, A Crystal-Analyzer Spectrometer. Nucl. Instrum. Methods Phys. Res., Sect. A 2009, 604, 719–728.

(89). Carpenter JM; Loong CK Elements of Slow-Neutron Scattering: Basics, Techniques, and Applications; Cambridge University Press: Cambridge, 2015.

(90). Mitchell PCH; Parker SF; Ramirez-Cuesta AJ; Tomkinson J Vibrational Spectroscopy with Neutrons: With Applications in Chemistry, Biology, Materials Science and Catalysis; World Scientific Publishing Company, 2005.

(91). Kresse G; Furthmüller J Efficient Iterative Schemes for Ab initio Total-Energy Calculations using a Plane-Wave Basis Set. Phys. Rev. B: Condens. Matter Mater. Phys 1996, 54, 11169–11186.

(92). Henkelman G; Uberuaga BP; Jónsson H A climbing image nudged elastic band method for finding saddle points and minimum energy paths. J. Chem. Phys 2000, 113, 9901–9904.

(93). Infrared/Terahertz Magneto Optics in DC Fields website. https://nationalmaglab.org/user-facilities/dc-field/dcfield-techniques/magneto-optics-ir-thz-dc.

(94). Clark RJH; Dines TJ Electronic Raman Spectroscopy. In Advances in Infrared and Raman Spectroscopy, Clark RJH, Hester RE, Eds.; Heyden & Son: London, 1982; Vol. 9, pp 282–360.

(95). Long DA Normal and Resonance Electronic and Vibronic Raman Scattering. The Raman Effect. A Unified Treatment of the Theory of Raman Scattering by Molecules, 1st ed.; Wiley, 2001; pp 289–302.

(96). Kiel A; Porto SPS Selection rules for the electronic Raman effect. J. Mol. Spectrosc 1969, 32, 458–468.

(97). Azuah RT; Kneller LR; Qiu Y; Tregenna-Piggott PLW; Brown CM; Copley JRD; Dimeo RM DAVE: A Comprehensive Software Suite for the Reduction, Visualization, and Analysis of Low Energy Neutron Spectroscopic Data. J. Res. Natl. Inst. Stand. Technol 2009, 114, 341–358. [PubMed: 27504233]

(98). Space Group 163: $P\overline{3}1c$. A Hypertext Book of Crystallographic Space Group Diagrams and Tables; Birbeck College, 1999. http://img.chem.ucl.ac.uk/sgp/large/163a.htm.

(99). Kresse G; Joubert D From Ultrasoft Pseudopotentials to the Projector Augmented-Wave Method. Phys. Rev. B: Condens. Matter Mater. Phys 1999, 59, 1758–1775.

(100). Blöchl PE Projector Augmented-Wave Method. Phys. Rev. B: Condens. Matter Mater. Phys 1994, 50, 17953–17979.

(101). Perdew JP; Burke K; Ernzerhof M Generalized Gradient Approximation Made Simple. Phys. Rev. Lett 1996, 77, 3865–3868. [PubMed: 10062328]

(102). Fu Y; Huang Z; Wang X; Ye L The Strong Correlation of the 4f Electrons of Erbium in Silicon. J. Phys.: Condens. Matter 2003, 15, 1437–1444.

(103). Deilynazar N; Khorasani E; Alaei M; Javad Hashemifar S First-Principles Insights into f Magnetism: A Case Study on some Magnetic Pyrochlores. J. Magn. Magn. Mater 2015, 393, 127–131.

(104). Klimeš J; Bowler DR; Michaelides A Chemical Accuracy for the Van der Waals Density Functional. J. Phys.: Condens. Matter 2010, 22, 022201. [PubMed: 21386245]

(105). Togo A; Tanaka I First Principles Phonon Calculations in Materials Science. Scr. Mater 2015, 108, 1–5.

(106). Phonopy website. https://atztogo.github.io/phonopy/index.html.

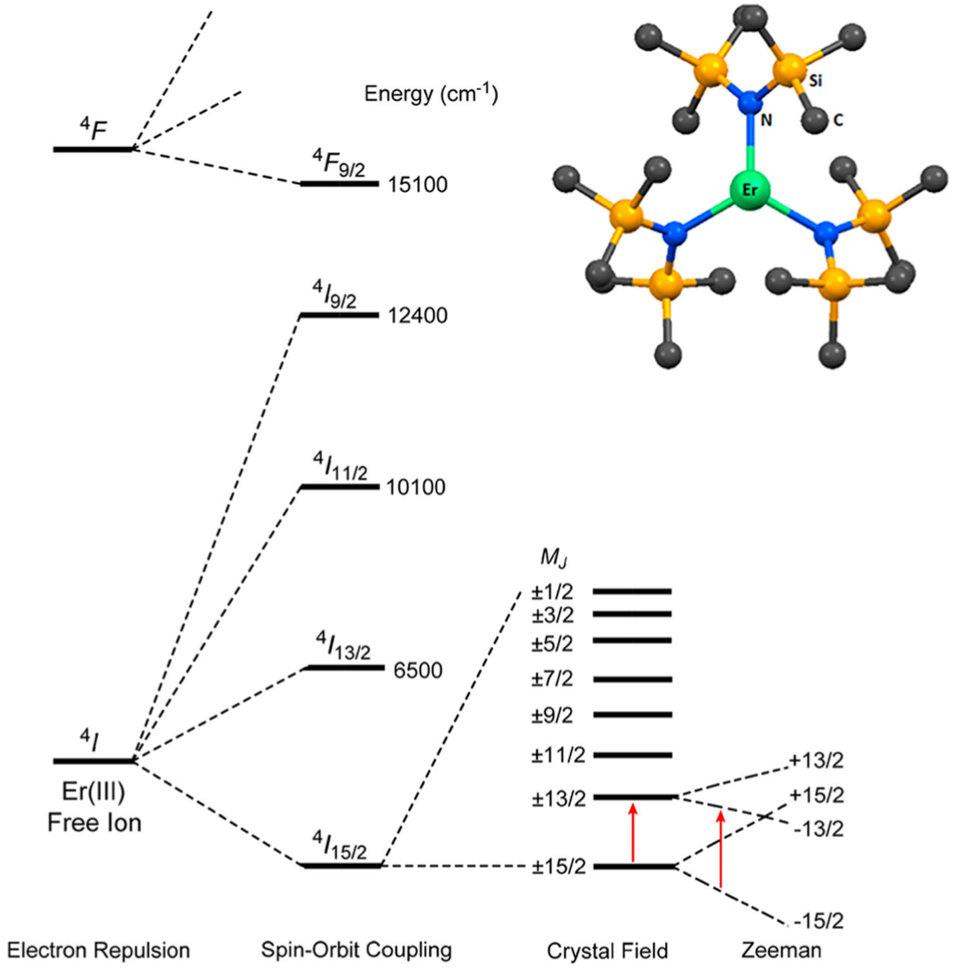

Figure 1.

(Top right) Structure of 1. Atom labels are Er (green), N (blue), Si (orange), and C (dark gray). (Bottom) Electronic interactions in an Er^{3+} ion due to electron repulsion, spin–orbit coupling, and crystal-field contributions. Red arrows represent the relative energies of the $M_J = \pm 15/2 \rightarrow \pm 13/2$ transition at 0 T and the $-15/2 \rightarrow -13/2$ transition under applied magnetic fields. It should be noted that labeling the crystal-field states by a single-eigenvector component M_J here is an approximation, as Jank et al. pointed out.[30] The labeling here does not include, e.g., third-order terms in the crystal-field Hamiltonian which may mix some of the states here.

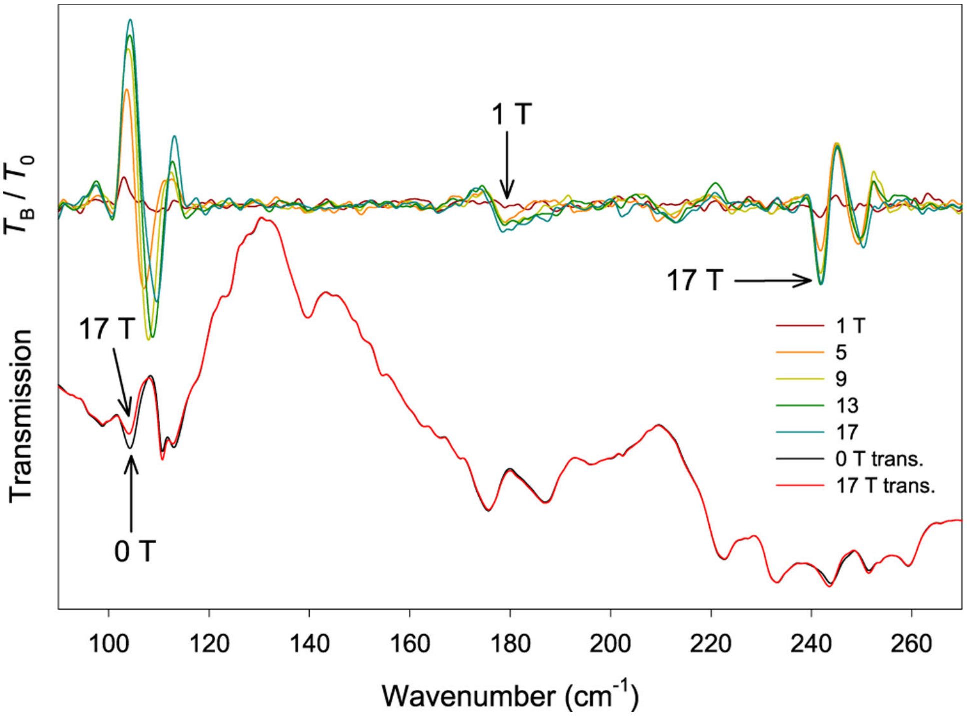

Figure 2.

(Bottom) Far-IR transmission spectra of a crystal sample of 1 at 0 T (black) and 17 T (red). (Top) Transmission normalized to the zero-field spectrum T_B/T_0 at 1, 5, 9, 13, and 17 T.

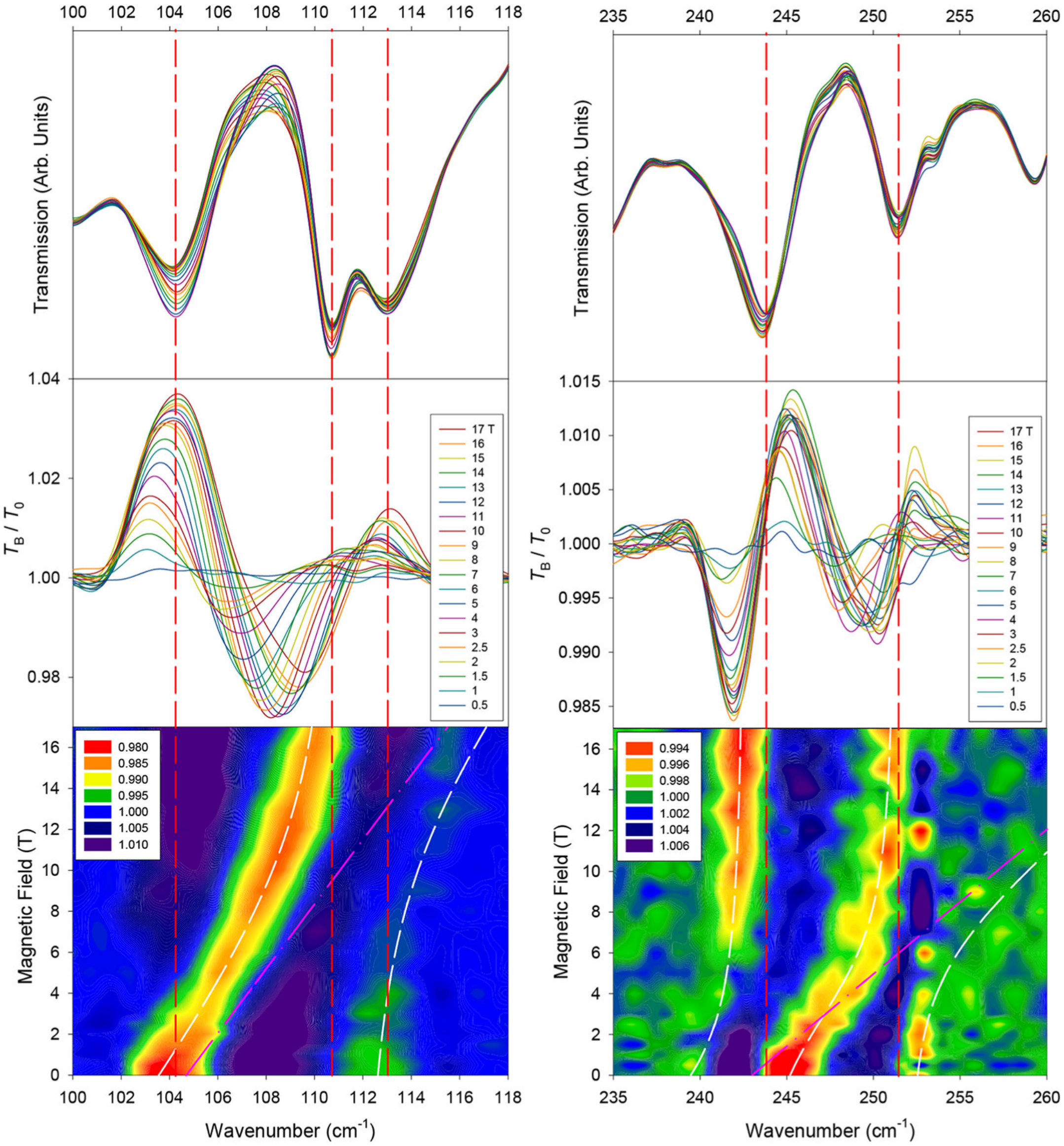

Figure 3.

Far-IR spectra in the vicinity of magnetic excitations (left) ν_1 and (right) ν_3 in a crystal sample of 1. (Top) Raw transmission. (Middle) Transmission (T_B) normalized to the zero-field spectrum (T_0). (Bottom) Contour plot of the normalized transmission (by average). White lines represent results of the Spin–Phonon coupling fit. Pink lines represent the shift of the uncoupled magnetic peak used for the coupling parameters E_{sp}. Vertical red lines indicate approximate zero-field positions of dominant phonon excitations.

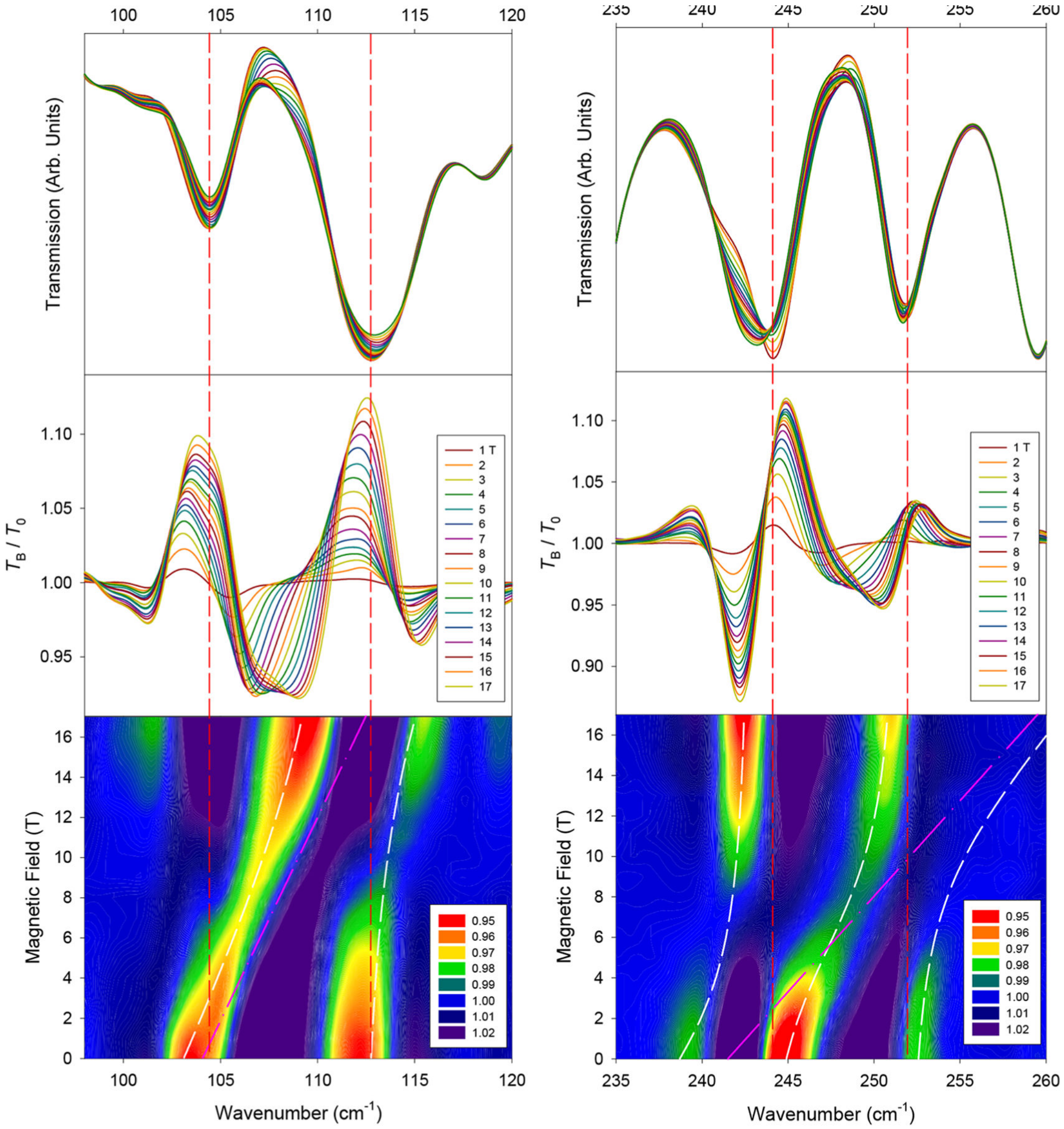

Figure 4.

Far-IR spectra in the vicinity of magnetic excitations (left) ν_1 and (right) ν_3 in a powder sample of 1. (Top) Raw transmission. (Middle) Transmission (T_B) normalized to the zero-field spectrum (T_0). (Bottom) Contour plot of the normalized transmission (by average). White lines represent results of the Spin–Phonon coupling fitting. Pink lines represent the shift of the uncoupled magnetic peak used for the coupling parameters E_{sp}. Vertical red lines indicate approximate zero-field positions of dominant phonon excitations.

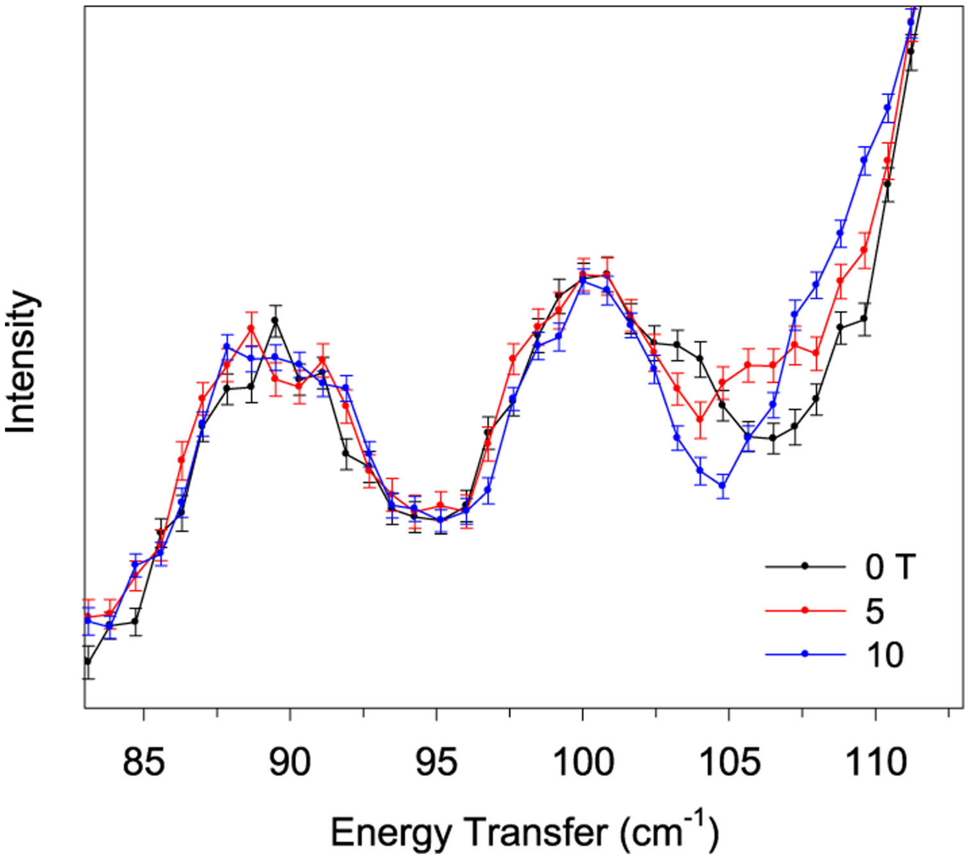

Figure 5.

INS spectra (DCS) at 1.7 K at 0 (black), 5 (red), and 10 T (blue). Error bars indicate ±1σ. The spectra in the complete energy transfer range (10–140 cm^{-1}) and a contour plot of the normalized scattering intensity (by average) are given in Figure S9. Unlike the transmittance far-IR spectra in Figures 2 and 3 and Figures S3–S5, the INS peaks in Figures 4–7 are pointed upward.

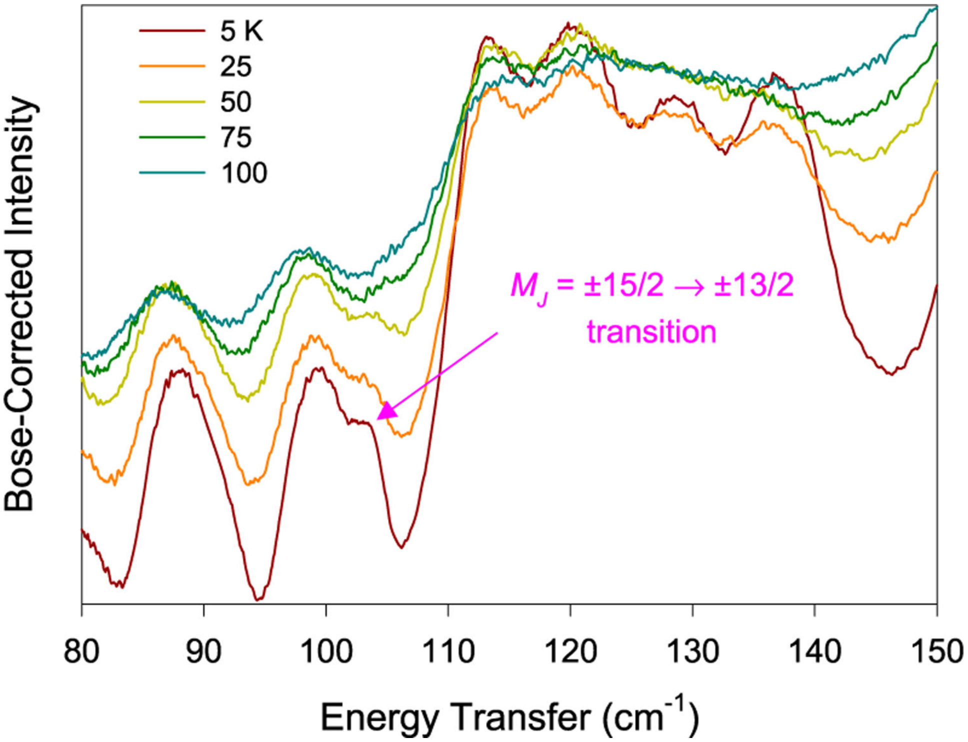

Figure 6.

Bose-corrected forward scattering INS spectra of 1 taken at VISION at different temperatures.[51,79]

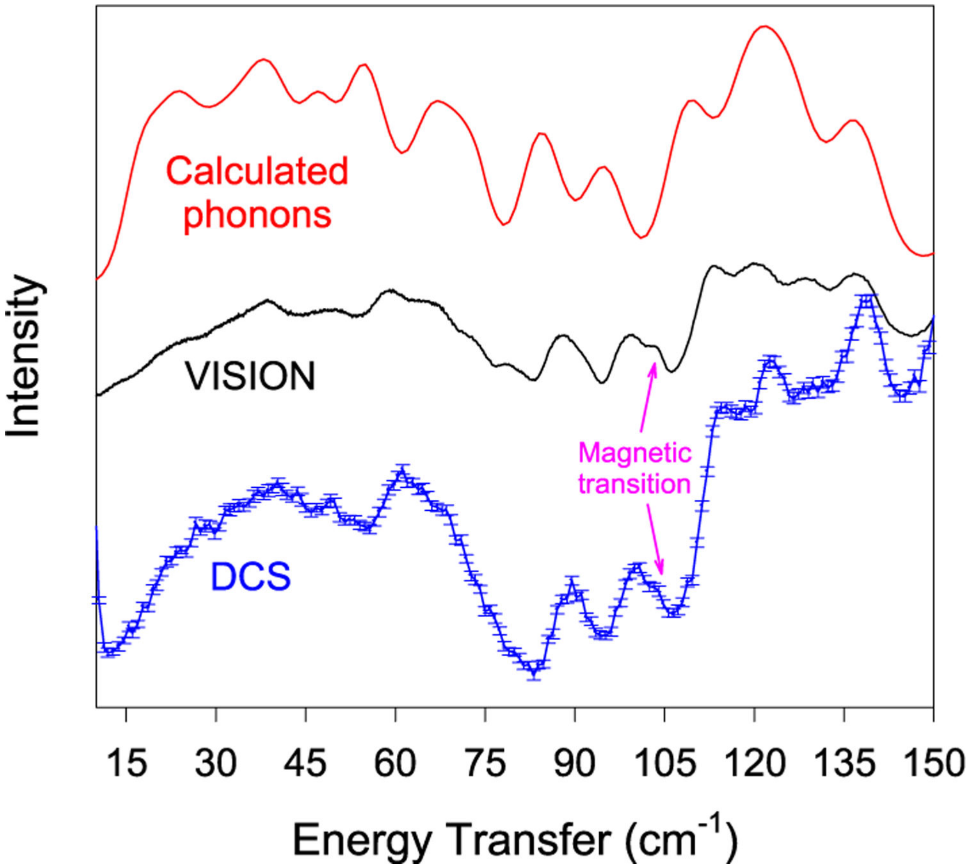

Figure 7.

Calculated and experimental INS spectra of 1 at 5 K in the 0–150 cm^{-1} range. (Top) Calculated phonons, (middle) VISION spectrum at 0 T, and (bottom) DCS spectrum at 0 T.

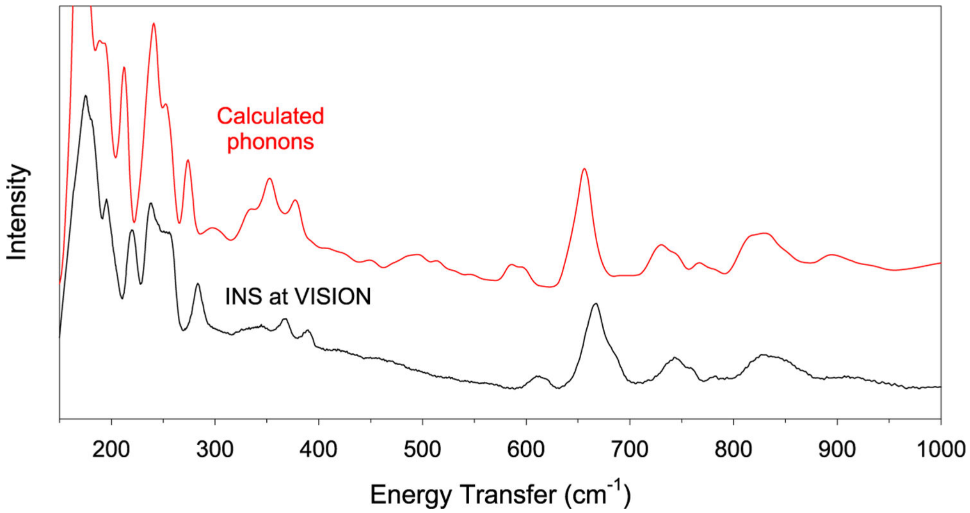

Figure 8.

INS spectrum (VISION) at 5 K in the 150–1000 cm^{-1} range in comparison with the calculated phonons. The 1000–3600 cm^{-1} range is given in Figure S11. Calculated excitation intensities of the entire range are shown in Figure S12. Calculated phonons in 1, including their symmetries and intensities, are given in Table S3.

Table 1.

Instrumental Properties and Sample Requirements for the FIRMS and INS Experiments in This Study

	feature	approximate energy range used (cm^{-1})	magnet used	temperatures (K)	amount of the sample used	location
far-IR	Bruker Vertex 80v FT-IR spectrometer	from 20 to 700	17 T	~4.6	5–10 mg of singlecrystals coated with eicosane 5–10 mg of powders mixed in eicosane	National High Magnetic Field Laboratory (Maglab or NHMFL)
INS by DCS[78]	direct geometry[51] with a monochromic incident neutron beam	from ~12 to ~150	10 T	1.7	2.3 g packed in Hefilled aluminum can	NIST Center for Neutron Research (NCNR)
INS by VISION[79]	indirect geometry[51] with a white incident neutron beam (of all energies)	from ~10 to 20 (depending on the temperatures) to ~4000	no magnet	5, 25, 50, 75, 100	2.3 g (same sample as that used in DCS)	Spallation Neutron Source (SNS), Oak Ridge National Laboratory (ORNL)

Table 2.

Energies of Each Magnetic/Inter-Kramers-Doublet Transition[a]

transition	energy (cm^{-1}) by the "hotband" method[30]	energy (cm^{-1}) from the current work[b]
±15/2 → ±13/2 (ν_1)	110	104 (far-IR/INS)
±15/2 → ±11/2 (ν_2)	190	approximately 180(5) (far-IR)
±15/2 → ±9/2 (ν_3)	245	245 (far-IR)

[a] The ±15/2 → ±7/2 transition (ν_4), observed at 327 cm^{-1} by the indirect "hot-band" optical absorption technique, appears to be at 285 cm^{-1} in the FIRMS spectra (Figure S7).

[b] The errors for the energies are estimated to be ca. 1 cm^{-1} (Supporting Information).